

The PELskin project—part I: fluid–structure interaction for a row of flexible flaps: a reference study in oscillating channel flow

Julien Favier  · Cuicui Li · Laura Kamps · Alistair Revell ·
Joseph O'Connor · Christoph Brücker

Received: 23 February 2016 / Accepted: 24 August 2016
© Springer Science+Business Media Dordrecht 2016

Abstract Previous studies of flexible flaps attached to the aft part of a cylinder have demonstrated a favourable effect on the drag and lift force fluctuation. This observation is thought to be linked to the excitation of travelling waves along the flaps and as a consequence of that, periodic shedding of the von Kármán vortices is altered in phase. A more general case of such interaction is studied herein for a limited row of flaps in an oscillating flow; representative of the cylinder case since the transversal flow in the wake-region shows oscillating character. This reference case is chosen to qualify recently developed numerical

methods for the simulation of fluid–structure interaction in the context of the EU funded ‘PELskin’ project. The simulation of the two-way coupled dynamics of the flexible elements is achieved via a structure model for the flap motion, which was implemented and coupled to two different fluid solvers via the immersed boundary method. The results show the waving behaviour observed at the tips of the flexible elements in interaction with the fluid flow and the formation of vortices in the gaps between the flaps. In addition, formation of vortices upstream of the leading and downstream of the trailing flap is seen, which interact with the formation of the shear-layer on top of the row. This leads to a phase shift in the wave-type motion along the row that resembles the observation in the cylinder case.

J. Favier () · C. Li
Laboratoire de Mécanique, Modélisation et Procédés Propres (M2P2), CNRS UMR 7340, Aix Marseille Université, Marseille, France
e-mail: Julien.Favier@univ-amu.fr

L. Kamps · C. Brücker
Institute for Mechanics and Fluid Dynamics, TU Bergakademie, Freiberg, Germany

Present Address:
C. Brücker
Department of Mechanical and Aeronautical Engineering, City University, London, UK
e-mail: Christoph.Bruesser@city.ac.uk

A. Revell · J. O'Connor
School of Mechanical, Aerospace and Civil Engineering (MACE), University of Manchester, Manchester, UK
e-mail: alistair.revell@manchester.ac.uk

Keywords Immersed boundary · Flexible canopy · *Monami*

1 Introduction

The wave behaviour of arrays of flexible structures (hairs, flaps, filaments) induced by a cross flow is an active area of research interest for a range of disciplines, and has been described in many studies [9, 16, 17, 22, 23]. This waving motion is most commonly referred to as *Honami* in the case of terrestrial canopies and *Monami* for aquatic canopies.

Of particular interest to flow control, a wave-type motion along rows of flexible structures has been observed in the wake of bluff bodies, where such flexible structures are attached to the aft part. The hairs interact with the unsteady wake flow and show the emergence of travelling wave-like motion patterns [5]. Experimental studies of flow past cylinders with attached hairs proved the potential for these structures to modify the shedding cycle [15]. The study showed a characteristic jump in the shedding frequency at a critical Reynolds number of $Re_c \approx 14,000$ when comparing to the classical behaviour of a plain cylinder wake flow. The analysis of the motions of the hairy-flaps showed that for $Re = Re_c$ the amplitude of the flap motion is considerably increased and a characteristic travelling wave-like motion pattern could be observed along the row of flaps. As a consequence, the presence of the hairy flaps alter the phase within the vortex shedding cycle such that the transverse dislocation—i.e. the transverse distance from the centerline—of the shed vortices is reduced [15]. Accordingly, the vortices are not arranged in a classical zig-zag pattern of the Kármán vortex-street, but rather they are shed in a row along the centerline ($y = 0$). These observations provided the motivations for the recent EU funded ‘PELskin’ project¹, wherein a small consortium of partners² focussed on investigating the potential amelioration of aerodynamic performance via a Porous and ELastic (PEL) coating. The objective being to elucidate the potential for passive structures to reconfigure/adapt to the separated flow, thereby directly changing the near-wall flow and the subsequent vortex shedding, which can lead to reduced form drag by decreasing the intensity and the size of the recirculation region.

A further investigation of the physical mechanisms involved in the fluid structure interaction within the rows of flaps requires a more general setup, so as to enable a detailed analysis of the flap behaviour under clearly defined conditions. This facilitates the parametric study of the interaction as a function of the

eigen-frequency, spacing and stiffness of the flaps. Such a case is proposed herein in form of an oscillating channel flow, where a limited row of flexible flaps is implemented. The selected configuration is simple enough to capture the essential characteristics of the coupled problem, and may also be considered to be quasi two-dimensional.

Experiments were carried out in a flow channel of square cross-section where fluid is driven by an oscillating piston along a row of 10 flexible flaps at a peak Reynolds-number of approximately 120. The numerical framework is based on the Immersed Boundary method coupled to a flow solver, to treat the moving boundaries on a fixed Cartesian grid. Two fundamentally different fluid solvers were used to compare their quality in comparison to the experimental data and judge the proper choice for further investigations of such coupled problems. The first is a finite difference code based on Navier–Stokes equations and the second one is a code employing the lattice Boltzmann method. The dynamics of the flexible elements is modelled using the Euler–Bernoulli equations, as it is done in [12] and [7]. Conclusions to this work will be drawn in Sect. 6.

2 Experimental set-up and methods

The oscillating channel flow is generated in a long tube of squared cross-section with diameter $L = 6\text{ cm}$ (cross-section $6\text{ cm} \times 6\text{ cm}$, or $3H \times 3H$, in terms of the flap length H) which is filled with liquid and is connected at the upstream end to a piston drive unit and at the downstream end to a basin (Fig. 1). As working fluid we use a mixture of water and glycerin to adjust the viscosity of the flow. This allows us to vary the characteristic numbers of the flow such as the Reynolds- and Wormersley-number across a wider range. The piston is able to run at maximum flow amplitudes of 16 cm of bulk fluid at oscillations frequencies of 1 Hz . All parts of the tube are made of transparent perspex to ensure optical access to the flow. The following results were obtained with a glycerine-water mixture of volume-ratio 80/20 resulting in a kinematic viscosity of $\nu = 100 \times 10^{-6}\text{ m}^2\text{ s}^{-1}$ at room temperature and a density of $\rho_f = 1.2\text{ g cm}^{-3}$.

In the centre of the tube is an insert, which contains a row of 10 flexible flaps ($d = 1\text{ mm}$ thick, length

¹ <http://www.transport-research.info/project/pel-skin-novel-kind-surface-coatings-aeronautics>.

² Aix Marseille Université, City University London, Wolfodynamics SRL, Technische Universität Bergademy Freiberg, The University of Manchester.

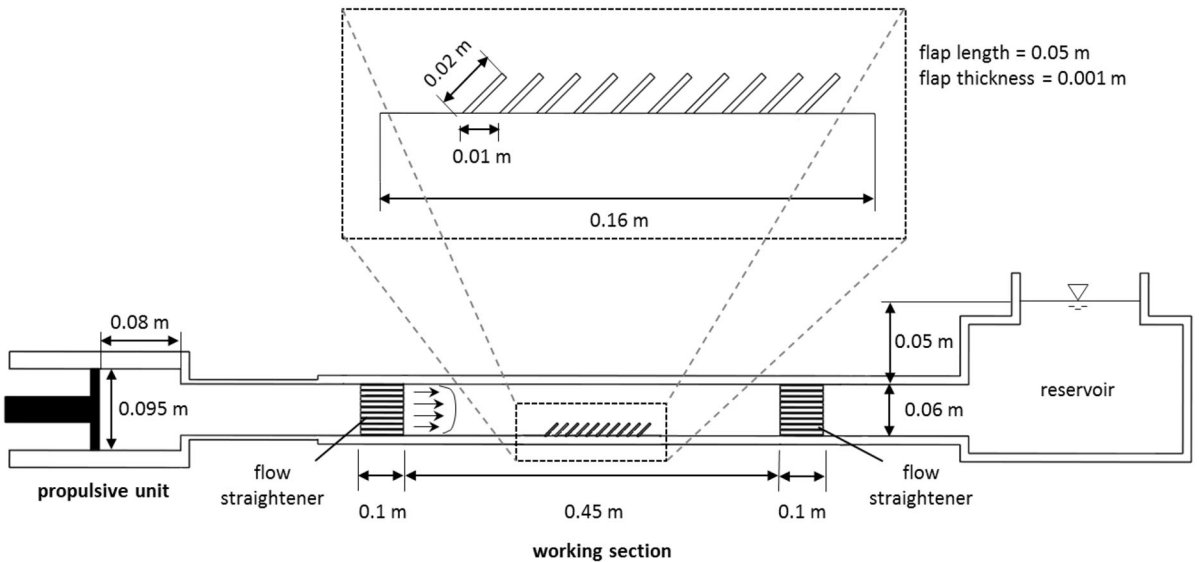


Fig. 1 Schematic view of the experimental working section

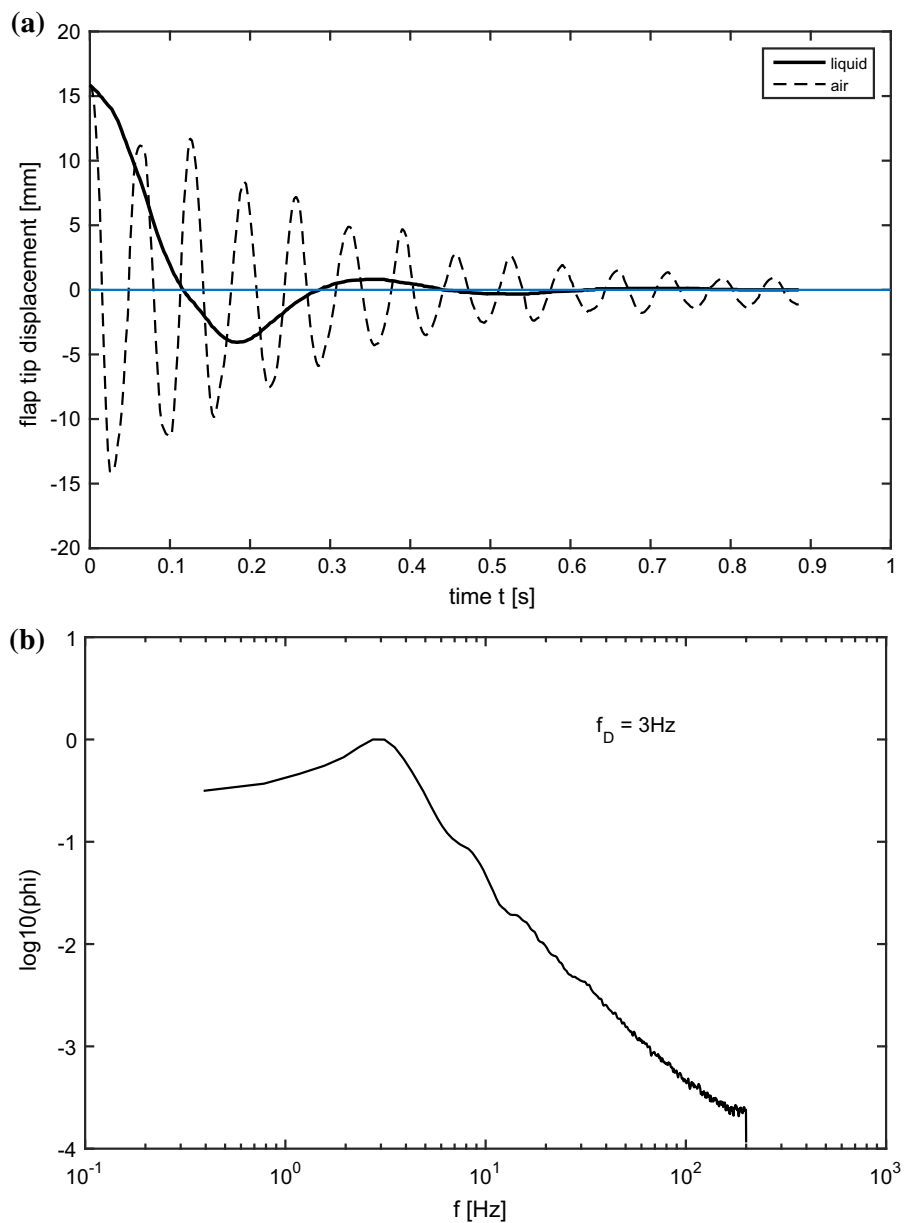
$H = 2 \text{ cm}$, span $B = 5 \text{ cm}$) that protrude into the flow. The interspacing between the flaps is set to 1 cm as the reference case. The flaps are made of silicone rubber (Elastosil RT 601, Wacker Chemie, Germany, Youngs modulus $E = 1.2 \text{ MPa}$, density $\rho_s = 1.2 \text{ g/cm}^3$) so that they are easily deflected by the flow. The flexural rigidity of the flaps k is calculated with $k = E \times I = 5 \times 10^{-6} \text{ Nm}^2$ (I is the second moment of area along the thin axis of the flap $I = Bd^3/12$). The density of the flaps ρ_s is equal to the density of the fluid ρ_f so that gravity is not contributing to the motion of the flaps in the experiments.

For characterization of the flap response, a step test was carried out in the liquid environment. The flap was deflected to a certain extend and was then released while recording the tip motion with a high-speed camera. The tip motion is shown in Fig. 2a). For comparison, the response curve in air is added, too. The latter shows the natural frequency of the flap at $f_n = 15 \text{ Hz}$ while for the damped case in liquid the damped frequency is $f_D = 3 \text{ Hz}$, see Fig. 2b). Therefore the damping coefficient D of the flap in the liquid is calculated from the relation $f_D = f_n \sqrt{(1 - D^2)}$ and results to $D = 0.98$.

The piston is controlled via a linear traverse (Moog Series) and performs a harmonic motion. To ensure an undisturbed flow within the centre of the flow channel from both sides we placed a honeycomb at the entrance

and exit of the tube as well as a smoothed transition insert from circular to squared cross-section. In the absence of flaps in the first instance, velocity profiles in the centre of the measurement chamber were measured with Particle Image Velocimetry. A high-speed camera (Phantom V12.1-8 G-M, Vision Research) recorded the flow evolution from the side while the centre plane was illuminated with a vertical light-sheet from below with a continuous laser (Ray Power 2000, Dantec). In addition to the PIV measurements, we used a special designed Schlieren setup with two larger lenses ($f = 400 \text{ mm}$) and illumination with a LED from the back in form of a point source for recordings of flap motion and shear-layer evolution. A special preparation of the flaps was required to achieve a good Schlieren image by means of differences in the refractive index of working liquid. This was intentionally generated by coating the flaps in the empty channel prior to the experiments with a thin water lining (refracting index of water $n_w = 1.33$). Then the channel was slowly filled with the working liquid, which has a higher refractive index than water ($n_l = 1.45$). When starting the oscillating flow, the water layer along the flaps is shed from the flaps along the shear-layers within the cavity between the flaps and in the shear layer formed along the top of the flap row. This allows us to visualize the shear-layer in a very illustrative way (see later discussion and Fig. 7).

Fig. 2 Step response of the flexible flap **a** motion in air (dashed line) and in the liquid (solid line). **b** Frequency response curve



3 Numerical method

The Immersed Boundary Method (IBM) is used to simulate the moving geometries of the flaps immersed in the unsteady fluid flow. Following this approach, the fluid equations are solved on a fixed Cartesian grid, which do not conform to the body geometry, and the solid wall boundary conditions are satisfied on the body surface by using appropriate volume forces [19–21]. In the context of the EU PELskin project, the fluid is solved using two different approaches, partly

as a function of the project planning and partly for the purpose of demonstrating the flexibility of the method.

3.1 Flow solver 1: lattice Boltzmann

In the first instance, the lattice Boltzmann method is used to simulate the fluid flow, which is based on microscopic models and mesoscopic kinetic equations; in contrast to Navier–Stokes which is in terms of macro-scale variables. The Boltzmann equation for the distribution function $f = f(\mathbf{x}, \mathbf{e}, t)$ is given as follows:

$$\frac{\partial f}{\partial t} + \mathbf{e} \cdot \nabla_{\mathbf{x}} f + \mathbf{F} \cdot \nabla_{\mathbf{e}} f = \Omega_{12}, \quad (1)$$

where \mathbf{x} are the spatial coordinates, \mathbf{e} is the particle velocity and \mathbf{F} accounts any external force; in the present work this force is the body force \mathbf{f}_{ib} applied to the fluid. Clearly this last term is very important as it will be used to convey the information between the fluid and the structure. The collision operator Ω_{12} is simplified using the Bhatnagar, Gross, and Krook (BGK) approach [2], where it is assumed that local particle distributions relax to an equilibrium state $f^{(eq)}$ in a single relaxation time τ :

$$\Omega_{12} = \frac{1}{\tau} (f^{(eq)} - f). \quad (2)$$

This equation is discretised and solved on the lattice, a Cartesian and uniform mesh in our case. At each point on the lattice, each particle is assigned one of a finite number of discrete velocity values. In our case we use the D2Q9 model, which refers to two-dimensional and nine discrete velocities, referred to by subscript i . The equilibrium function $f^{(eq)}(\mathbf{x}, t)$ can be obtained by Taylor series expansion of the Maxwell–Boltzmann equilibrium distribution [24].

Concerning the discrete force distribution needed to keep into account the body force \mathbf{f}_{ib} , here we use the formulation proposed by [10], as follows, where c is the lattice speed, $c_s = 1/\sqrt{3}$ is the speed of sound and ω_i are the weight coefficients, which take standard values. For further details the reader is referred to [6].

$$F_i = \left(1 - \frac{1}{2\tau}\right) \omega_i \left[\frac{\mathbf{e}_i - \mathbf{u}}{c_s^2} + \frac{\mathbf{e}_i \cdot \mathbf{u}}{c_s^4} \mathbf{e}_i \right] \cdot \mathbf{f}_{ib} \quad (3)$$

3.2 Flow solver 2: Navier Stokes

In this work we also use an incompressible Navier–Stokes solver with a staggered grid discretization [11]. In this case, both convective and diffusive fluxes are approximated by second-order central differences. The fractional time-step method is used for the time-advancement [4, 14], in the form of a second-order semi-implicit pressure correction procedure [13]. The alternating direction implicit method (ADI) is used for the temporal discretization of the diffusive terms, allowing to transform three-dimensional problem into three one-dimensional ones by an operator-splitting technique, while retaining the formal order of the

scheme. The code parallelization relies upon the Message-Passing Interface (MPI) library and the domain-decomposition technique.

The numerical strategy used to impose the desired zero velocity boundary condition at the solid surface (which is a solid and rigid wing) is the following. The predicted velocity \mathbf{u}^* , if first obtained explicitly, without the presence of the embedded boundary:

$$\mathbf{u}^* = \mathbf{u}^n - \Delta t \left[\mathcal{N}_l(\mathbf{u}^n, \mathbf{u}^{n-1}) - \mathcal{G}\phi^{n-1} + \frac{1}{Re} \mathcal{L}(\mathbf{u}^n) \right], \quad (4)$$

where \mathbf{u}^n is the divergence-free velocity field at time-step n , Δt is the time step, \mathcal{N}_l is the discrete non-linear operator, \mathcal{G} and \mathcal{D} are, respectively, the discrete gradient and divergence operators, \mathcal{L} is the discrete Laplacian, ϕ is a projection variable (related to the pressure field). The operators include coefficients that are specific to the time scheme used in this study, a three-steps low-storage Runge Kutta.

3.3 Immersed boundary method to couple flow solver to structure model

The presence of the solid geometry is imposed by using the IBM, via a process of interpolation and spreading [25]: \mathbf{u}^* is interpolated onto the embedded geometry of the obstacle, Γ , which is discretized through a number of Lagrangian marker points with coordinates \mathbf{X}_k :

$$\mathbf{U}^*(\mathbf{X}_k, t^n) = \mathcal{I}(\mathbf{u}^*) \quad (5)$$

At this stage, knowing the velocity $\mathbf{U}^*(\mathbf{X}_k, t^n)$ at location of the Lagrangian markers, a distribution of singular forces that restore the desired velocity $\mathbf{U}^d(\mathbf{X}_k, t^n)$ on Γ is determined as:

$$\mathbf{F}^*(\mathbf{X}_k, t^n) = \frac{\mathbf{U}^d(\mathbf{X}_k, t^n) - \mathbf{U}^*(\mathbf{X}_k, t^n)}{\Delta t}. \quad (6)$$

The singular surface force field given over Γ is then transformed by a spreading operator \mathcal{S} into a volume force-field defined on the Cartesian mesh points $\mathbf{x}_{i,j,k}$ surrounding Γ :

$$\mathbf{f}^*(\mathbf{x}_{i,j}, t^n) = \mathcal{S}[\mathbf{F}^*(\mathbf{X}_k, t^n)]. \quad (7)$$

At this stage, in the case of the lattice Boltzmann method, the force $\mathbf{f}^*(\mathbf{x}_{i,j}, t^n)$ is used directly as \mathbf{f}_{ib} in eqn 3 and the algorithm is completed. For the Navier

Stokes solver, some final steps are required as follows. First, the predicted velocity is re-calculated, using an implicit scheme for the viscous operator, adding the forces that accounts for the presence of the solid body:

$$\frac{\mathbf{u}^* - \mathbf{u}^n}{\Delta t} = -\mathcal{N}_l(\mathbf{u}^n, \mathbf{u}^{n-1}) - \mathcal{G}\phi^{n-1} + \frac{1}{Re}\mathcal{L}(\mathbf{u}^*, \mathbf{u}^n) + \mathbf{f}^* \quad (8)$$

Finally, the algorithm completes the time step with the usual solution of the pressure Poisson equation and the consequent projection step:

$$\mathcal{L}\phi = \frac{1}{\Delta t}\mathcal{D}\mathbf{u}^* \quad (9)$$

$$\mathbf{u}^{n+1} = \mathbf{u}^* - \Delta t\mathcal{G}\phi^n. \quad (10)$$

The key elements of the present IBM are the transformations between the Eulerian the Lagrangian meshes, which are carried out through the interpolation and spreading operators, \mathcal{I} and \mathcal{S} . These two operators are built using a method presented in [6, 21], which ensures that the interpolation and spreading are reciprocal operations, implying that the integral of the force is the same when computed in the Lagrangian or Eulerian frames. Important properties of the algorithm are the preservation of the global accuracy of the underlying differencing scheme, and the sharpness with which the interface is resolved. For further details the reader is referred to [21] and [6].

3.4 Model of flexible flap

Coming back to Eq. 6 defined on each Lagrangian marker, the term $\mathbf{U}^{dn+1}(\mathbf{X}_k)$ denotes the velocity value at the location \mathbf{X}_k we wish to obtain at time step completion. Those values are determined for each flap integrating in time the respective Euler–Bernoulli equation in non-dimensional form:

$$\frac{d\mathbf{U}^{dn+1}}{dt} = \frac{\partial}{\partial s} \left(T \frac{\partial \mathbf{X}_k}{\partial s} \right) - K_B \frac{\partial^4 \mathbf{X}_k}{\partial s^4} + Ri \frac{\mathbf{g}}{g} - \mathbf{F}_{ib} \quad (11)$$

Here, T is the non-dimensional tension of the flap and K_B is the non-dimensional flexural rigidity k/K_{Bref} . The reference quantities used for non dimensionalising the equations are: a reference tension $T_{ref} = \Delta\rho U_0^2$, the reference bending rigidity $K_{Bref} = \Delta\rho U_0^2 L^2$ and the reference Lagrangian forcing

$F_{ref} = \frac{\Delta\rho}{L\rho_f} U_0^2$. U_0 is the characteristic velocity of the fluid flow, $\Delta\rho$ is the difference in density per unit area of filament cross section between the filament ρ_s and the fluid ρ_f . Gravity effects are introduced via the Richardson number, $Ri = gL/U_0^2$, though in the following, gravity effects are only included for the validation case of the flap model without fluid. The closure of Eq. 11 is provided by the inextensibility condition that reads:

$$\frac{\partial \mathbf{X}_k}{\partial s} \cdot \frac{\partial \mathbf{X}_k}{\partial s} = 1 \quad (12)$$

This condition ensures that the flap length remains constant, and is satisfied using the tension values, which effectively act as Lagrange multipliers. The boundary conditions for the system (11–12) are $\mathbf{X} = \mathbf{X}_0$, $\frac{\partial^2 \mathbf{X}_k}{\partial s^2} = 0$ for the fixed end, and $T = 0$, $\frac{\partial^2 \mathbf{X}_k}{\partial s^2} = 0$ for the free end. The resulting set of equations are discretised using a staggered arrangement and solved using a Newton method, by a direct evaluation of the exact Jacobian matrix, which incorporates the given boundary values. More details can be found in [6].

4 Validation of fluid structure interaction

The validation is first performed for the model of flexible flap alone (pure solid), and subsequently the fluid solver is validated alone (pure fluid), by comparing with the experiments. The flow unsteadiness allows one to identify and characterize the time dependent dynamics of the oscillating flexible flaps.

4.1 Flap model without fluid

To check the consistency of the structure model, the motion of a hanging flap without ambient fluid and under a gravitational force is considered, as shown in Fig. 3a. The non-dimensional flexural rigidity is set to $K_B = 0$, so that a flexible flap (a pendulum) with an initial angle $\theta_o = 2^\circ$ is examined. The time evolution of the coordinate of the free extremity in the x-direction (Δx) is monitored by setting the gravity to a value equivalent to $Ri = 10$. Figure 3b shows that the time evolution of the free extremity position of the flap using the present model is in good agreement with the analytical solution which can be obtained under the small angles assumption [6].

4.2 Fluid simulation without flap

A fluid simulation without flap is then conducted in a computational domain which is set to $22H \times 3H$ (H is the height of flexible flap), in streamwise (x) and vertical (y) direction respectively corresponding to the 2D case of the centerplane in the experimental flow channel. Periodic boundary conditions are imposed in x-direction, and no-slip conditions are applied on the upper and lower walls. The flow is driven by an oscillating flow, by sinusoidally varying the pressure gradient at a given flow frequency $f = 1.0$ Hz as following:

$$\frac{\partial p}{\partial x} = A \sin(2\pi f t) \quad (13)$$

The present simulation follows a Womersley velocity profile, in the same way as the analytical expression derived by [3] for a squared channel flow in the center-plane. Figure 4 indeed shows a good agreement between simulation, experiment and the analytical solution of [3] at the inlet through one flow oscillation cycle. The Reynolds number of the present simulation is $Re = U_{max}H/v = 120$, based on the characteristic streamwise velocity U_{max} and the flexible flap height H . The Womersley number defined with the channel diameter L is $\alpha = L\sqrt{2\pi f/v} = 15$.

4.3 Fluid structure interaction

A two-way fluid structure interaction configuration is considered at the same dimensions and same boundary conditions as in Sect. 4.2. The flexible flaps are mounted on the bottom wall of the channel. Figure 1 shows the experimental setup, where the same ratio 3.0 of channel height over flap length, the same flow velocity profile and flow frequency, as the simulation

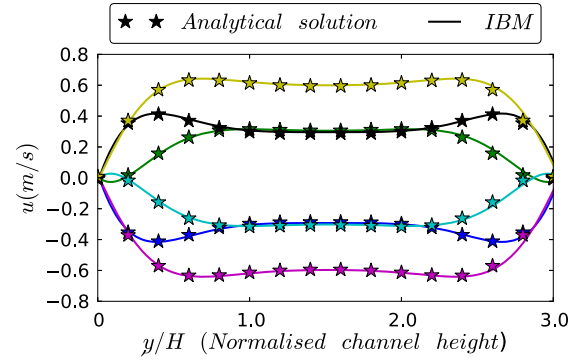


Fig. 4 Womersley velocity profiles at inlet position at different instants through one flow oscillation cycle (IBM: present work using immersed boundary method)

case, are adopted. In the first instance a refinement study was undertaken as shown in Fig. 5. The metric L refers to the number of Lagrangian markers along each flap, and it is obvious that even for low resolutions the accuracy is good. A value of 35 Lagrangian points per cilia is taken for subsequent computations. Also shown in Fig. 5, is the L2 norm of the convergence, with respect to the prediction from the finest level of refinement ($L = 40$). It is clear that the numerical method is of 2nd order accuracy during these computations.

Figure 6 provides a comparison of tip positions of flaps in x direction obtained from both flow solvers, the experimental results are also plotted for comparison. The initial observation is that both flow solvers return almost identical results for this case, providing grounds for cross-validation of the two implementations. Minor differences are likely to be due to differences in numerical settings, as well as the impact of the significantly different nature of the two methodologies; for example the LBM is effectively a compressible solver, while the current N-S method is

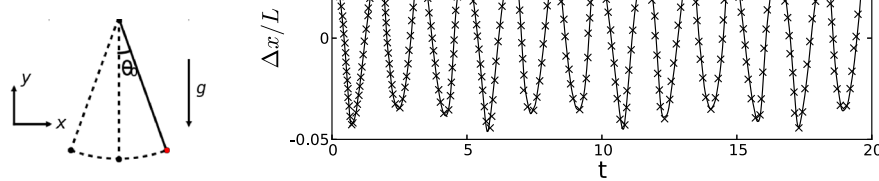


Fig. 3 Motion of the hanging flexible flap under gravity (without fluid) without bending term and with an initial angle of $\theta_0 = 2^\circ$. **a** Initial position of the flexible flap. **b** Time evolution

of the tip position Δx , with respect to the position in x of its equilibrium position. Present solution: —, analytical solution: x

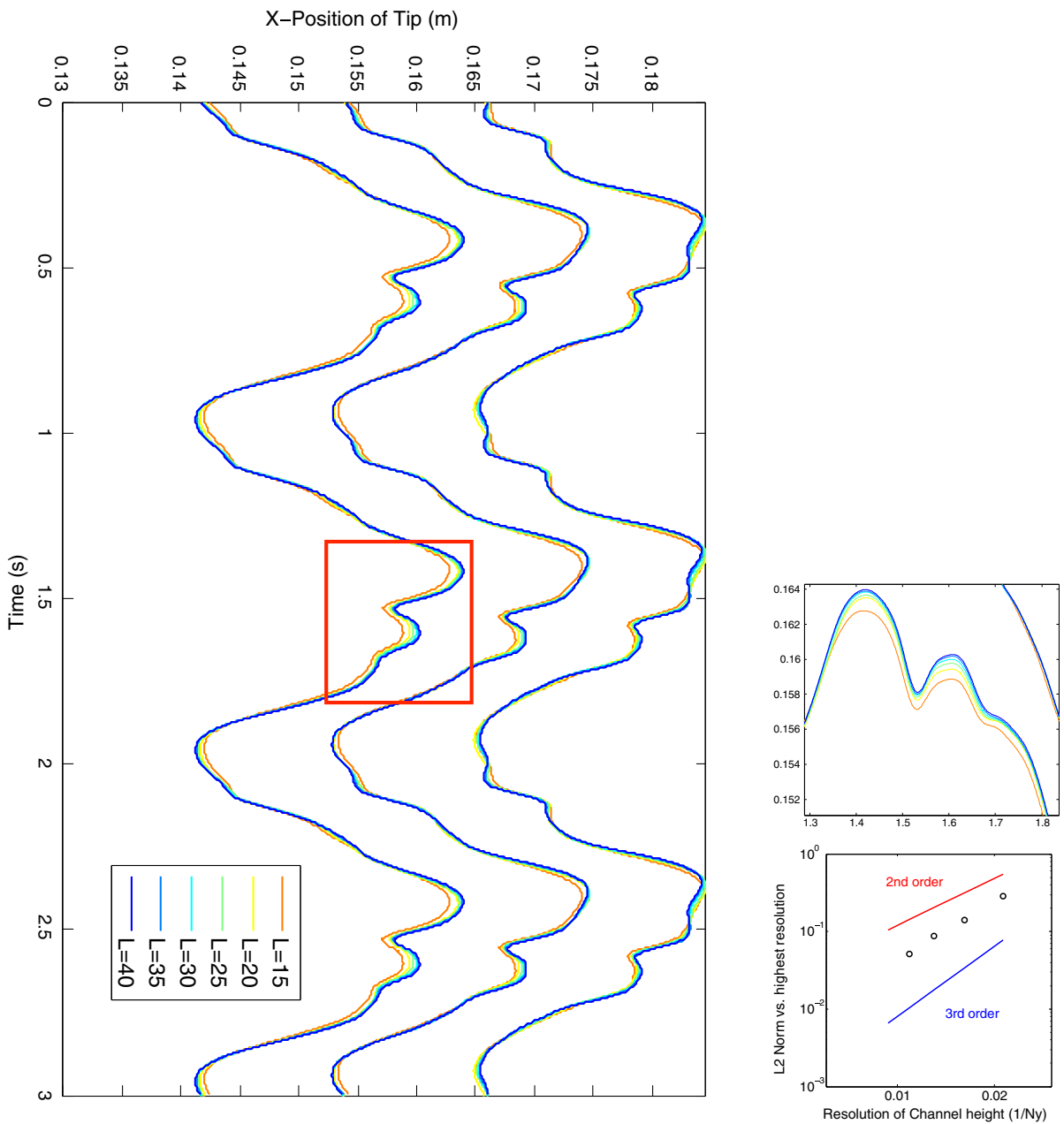
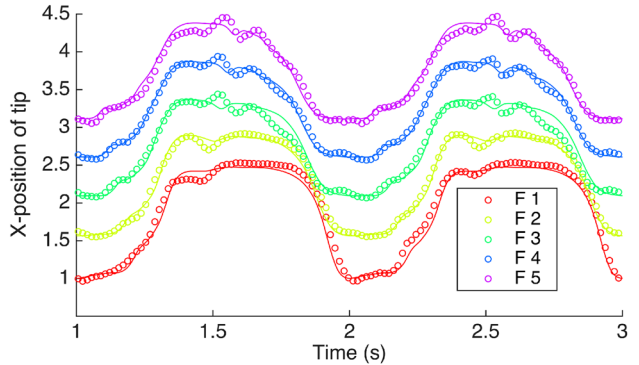


Fig. 5 Refinement study of coupled FSI solver (using LBM), showing tip displacement (x coordinate) of flap in centre of array for increasing flap resolution. Also shown are zoom view (*top right*) and L2 convergence (*red line* order 2, *blue line* order 3). (Color figure online)

incompressible. The second observation is with respect to the experimental results, and again, the agreement is strong. The main amplitude is well captured, although a small ‘kick’ in the profile of the first flap (F1) is missed by both solvers. This could be due to differences in the approximation of the structural parameters of the model, which slightly

differ from experiments to numerics. Also, the 2D approximation made in the numerical solvers may play a role on this phenomenon. However, towards the more centrally located flaps, the agreement improves, with finer detail of the tip motion at the oscillating extremities agreeing notably well with the experimental data.

Fig. 6 Tip positions of flap in x-direction within three flow cycles. —: numerical results from LBM; —: numerical results from N-S solver, $\circ \circ$: experiment. The letters F_i indicate the flexible flap number i



Further validation can be obtained from analysis of instantaneous flow velocity vector (u, v) are as provided in Fig. 7a–d for the numerical results and Fig. 7e–h for the corresponding experimental results. Again the indication is for an accurate prediction of tip location, and where streaklines are observable in the experimental results, numerically predicted contours of velocity are in good agreement also. The roll-up of shears layer can be seen due to the relative motion of the forward mean flow and the backward motion of the flap tips and vice versa. This will be investigated in more detail in the following section.

5 Numerical results

We start by investigating and elucidating the principle flow mechanisms identified in this case, and focus on two key aspects; the identified phase lag of the flaps, and the cyclic generation of coherent structures.

5.1 Phase lag

Forced by the driving motion of the fluid, the flaps individually move at the same frequency as the flow. However, there is a clear phase lag between adjacent flaps as seen in the normalized flap tip position, see Fig. 8. The displacements of each flap tip levels off differently in time and they reach different maximum and minimum values of $\Delta x/H$. Δt_1 and Δt_2 are defined as the time differences between two successive time instants when the flap tip reaches the position of its fixed extremity in x-direction ($\Delta x = 0$). Due to the phase lag of flap response, which is different depending on the flap location on x-direction, the values of Δt_1 and Δt_2 are different for each flap.

This phase lag between adjacent elements has already been observed in several research works on waving motions of flexible plants, and plays an important role in the emergence of the coherent waving motion of plants. It is known as *Honami* in the case of resonant waving of wheat stalks for instance [8], or *Monami* in the case of aquatic waving plants [17]. Despite numerous literature work associated with *Honami/Monami*, little qualitative information [8] and no quantitative data are available regarding the phase lag of these structures. On the other hand, a similar wave-type motion pattern was observed in the case of flexible flaps attached to the aft part of cylinder and it was found that this motion pattern plays an important role in the modification of the wake [15]. More recent work focussing on an infinite array of flaps demonstrated that a Reynolds dependence of the phase lag was associated with the size of the recirculating flow between successive flaps, but the study was limited to infinite periodic arrays of flaps [18]. Therefore the present results in the oscillating channel flow can make a significant contribution to the understanding of this phenomenon.

5.2 Detection of coherent eddies

To investigate the flap dynamics and the phase lag evolution between adjacent flaps, snapshots of instantaneous velocity field (u, v) through one flow cycle ($T = 1.0\text{s}$) are provided in Fig. 9. Results reveal that flap 1 begins to deflect from its vertical position at $t = 0.26\text{ s}$ in Fig. 9a, and finally recovers this initial position at $t = 1.26\text{ s}$ in Fig. 9j.

Just afterward the start of the cycle, at $t = 0.5\text{ s}$ of Fig. 9b, the bulk flow velocity becomes positive (left to right) and a vortex is formed at the right side of flap

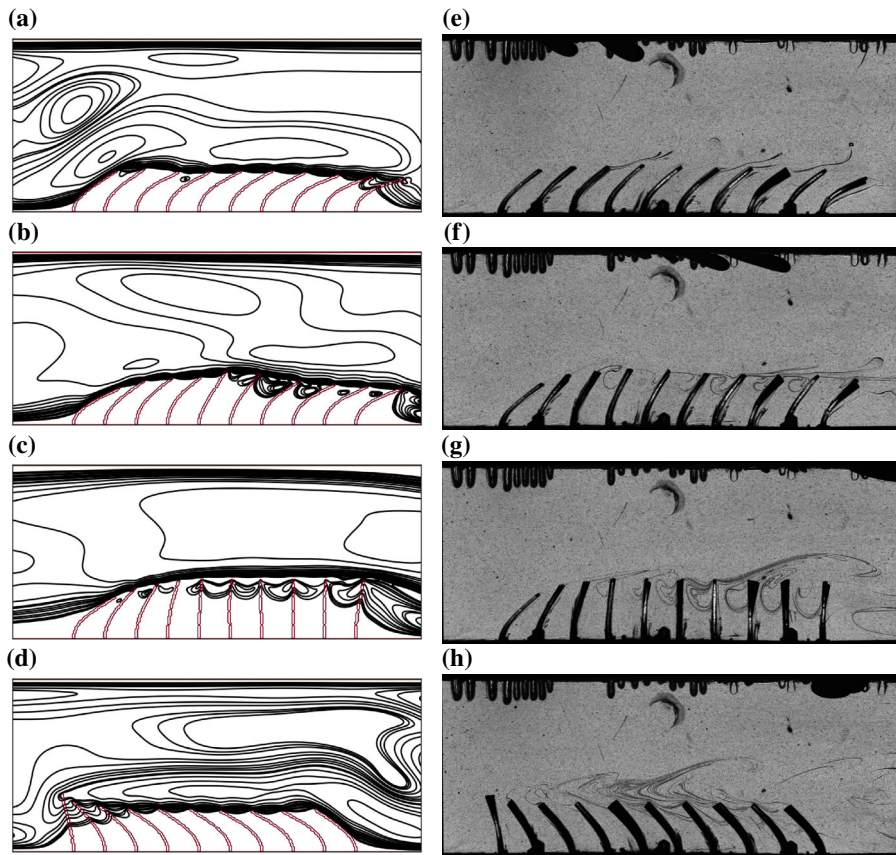
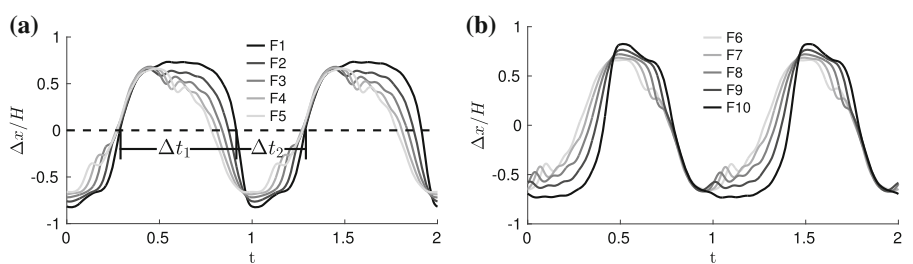


Fig. 7 Evolution of the flow over a half-period of the oscillation cycle. **a–d** Contours of instantaneous flow velocity vectors (u, v) obtained by numerical simulation; **e–h** experimental

snapshots of Schlieren images obtained at the same instant as in the numerical simulation

Fig. 8 Superimposed normalized tip deflections Δx of flexible flaps for **a** F1–F5, **b** F6–F10



layer, as shown at $x \approx 14.25$ in Fig. 9c. Although initially small this vortex quickly grows, as shown in Fig. 9d–e. Consequently a region of negative streamwise velocity is formed near the lower wall downstream of the flaps, and very quickly induces a large deflection of the flexible flaps near to the right side of the array. The largest deflection is experienced by flap 10, while deflections are reduced progressively towards the channel centre, i.e. for flaps 9 to 6.

During the same period, the impinging cross flow induces a large deflection of flap 1, which is initially notably greater than flaps 2–5. As the flow evolves this deflection is transmitted through flaps 2 and 3, as shown in Fig. 9c, d. This wave-like motion results in a

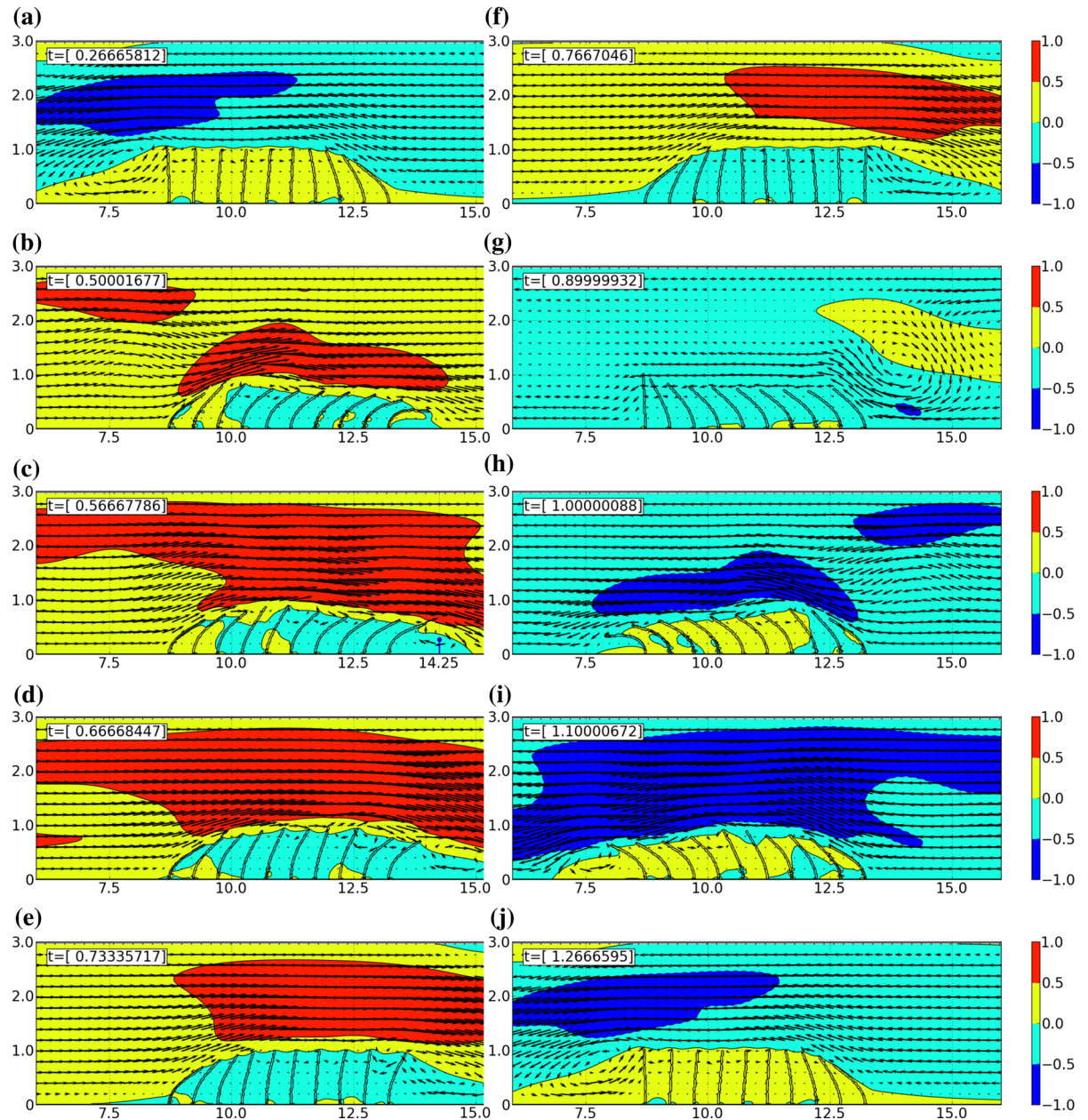


Fig. 9 Instantaneous flow velocity vectors (u, v) represented by arrows through one flow oscillation cycle. The channel dimension is normalized by the flap height H . The colormaps correspond to the values of contours of streamwise velocity u . (Color figure online)

smoothly varying phase lag, as also indicated on Fig. 8a for the approximate range $0.45 < t < 0.65$.

From Fig. 9f onwards, the bulk flow velocity becomes negative (right to left), and the reverse mechanism is observed.

Under the driving motion of the oscillating flow, the flexible flap motion is thus significantly influenced by

the presence of the vortex, which periodically appears near to both sides of the coating. Its presence is confirmed via comparison with experimental observation, as shown in Fig. 10.

Also, it appears that the temporal and spatial responses of the flexible flaps are closely related to their distances from the channel centre position in

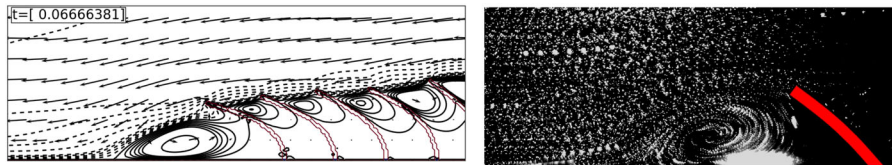
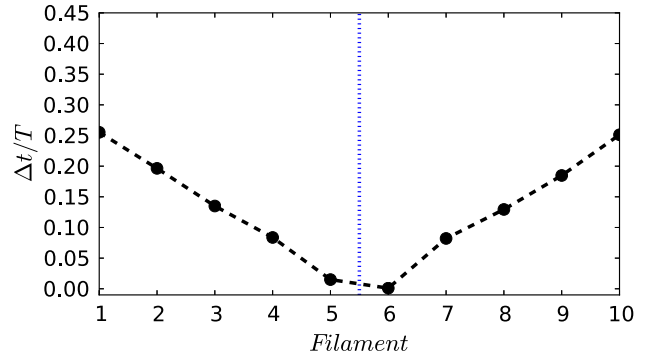


Fig. 10 (left) Instantaneous flow velocity vectors (u, v) represented by *arrows* and *contours* of streamwise velocity u . (right) Path lines of tracer particles in the corner of the flaps from experiment

Fig. 11 Phase difference ratio $\Delta t/T$ (T is the oscillating flow cycle). The x -axis indicates the flap positions in x -direction. The *vertical blue line* indicates the channel centre position of x -direction. (Color figure online)



streamwise direction. As shown in Fig. 11, this relationship is linear, i.e. the phase difference Δt ($\Delta t = \Delta t_1 - \Delta t_2$) of each flap tip position, normalized by the oscillating flow cycle T , is proportional to their distance to the channel centre in x -direction. The lack of symmetry reflects the initialisation of the flow, wherein the flaps are initially arranged vertically and undergo initial deflection to the right, via a positive bulk flow velocity.

Figure 12 shows several snapshots of instantaneous velocity field (u, v) and the corresponding instantaneous vorticity. The coherent vortex observed in Fig. 12a-d is clearly associated to large vorticity regions in Fig. 12e-h. From Fig. 9, it can be seen that the boundaries of the highlighted zones of uniform momentum pass through the cores of coherent vortices, which suggests an important link between coherent vortices and uniform-momentum zones, as it is also observed in the analysis performed in the experimental results of [1] and [17].

6 Conclusions

The physical mechanisms involved in the two-way interaction between an incompressible oscillating channel flow and a coating made of flexible flaps

have been investigated in the present work. A Navier Stokes solver and a Lattice Boltzmann solver have been used, and it is found that both methodologies are in principle good agreement with the results of experiment at the same conditions, for similar CPU costs. Thus, the incompressible or compressible nature of the solvers does not play any role in this configuration involving flexible structures immersed in an unsteady flow.

It is shown that a cyclically generated coherent vortex, occurring alternatively near the entrance and the exit of the flap row, is the primary cause leading to the smoothly varying phase difference of adjacent flaps. This coherent vortex generation cycle is expected to hold in general for the case of a finite array size, since it depends on entrance and exit effects; i.e. flow impingement on the upstream end of the array and recirculation on the downstream end. Where flap rows are infinite in length, such entrance and exit effects are expected to vanish, and interaction would be driven solely by incoherence in dynamic response of the flexible structures either by variation in stiffness or near the resonant excitation where phase relationship is lost.

The observed effect is comparable to the situation of flaps in the aft part of a cylinder in cross-flow. The flaps interact with the roll-up of the shear layer which

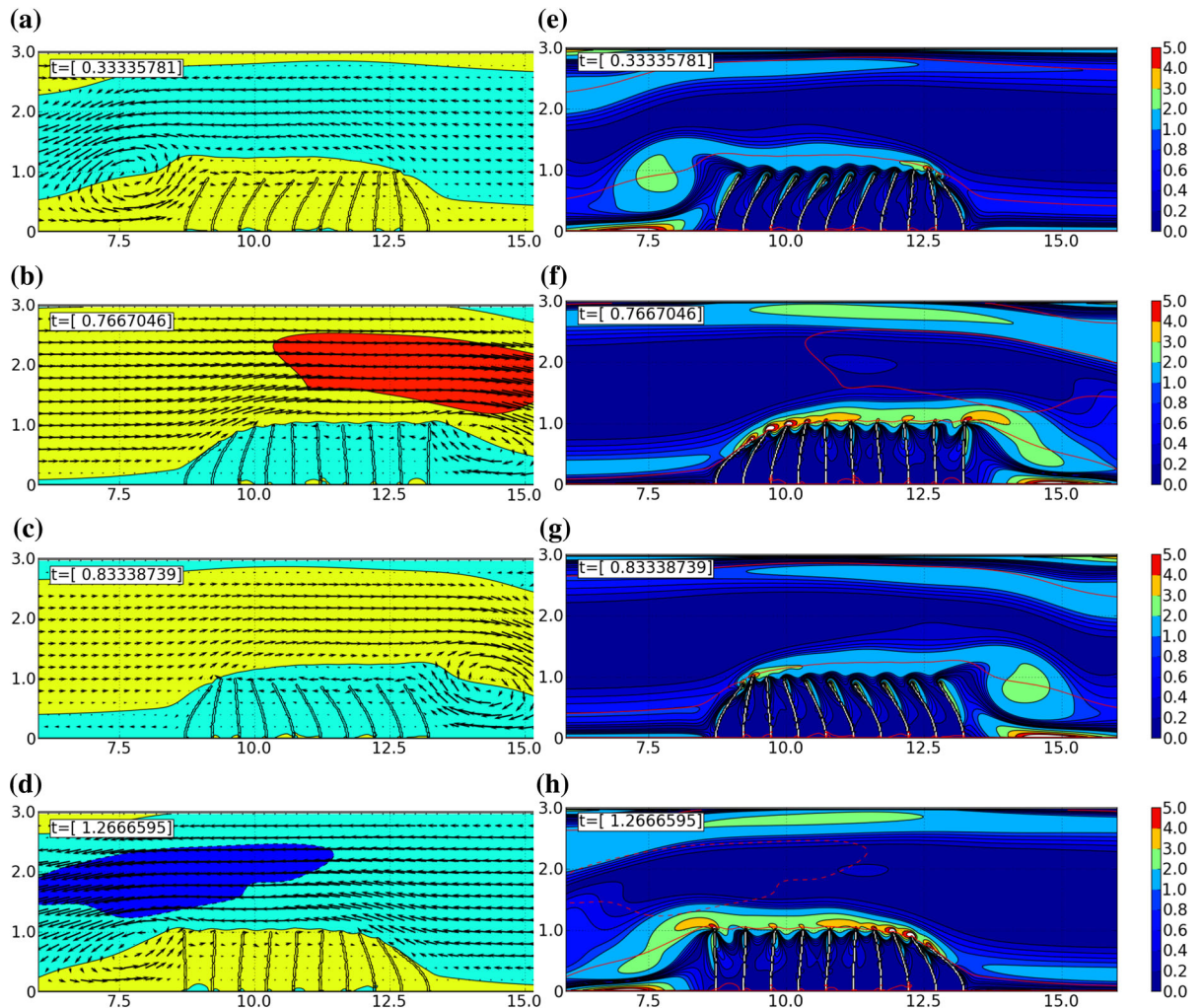


Fig. 12 a–d Instantaneous flow velocity vectors (u, v) represented by arrows and color contours of streamwise velocity u ; e–h Color contours of instantaneous vorticity. The boundaries between uniform-momentum zones are shown by red lines. (Color figure online)

leads to a phase shift in formation of the von Karman vortices. This roll-up starts along the lateral side-walls of the cylinder and vorticity is then swept along the row of the flaps in transversal direction towards the inner part of the row, similar as in the case discussed herein. Therefore the observed travelling wave-type motion of the flaps in the cylinder wake [5, 15] is a result of the phase-shift between neighbouring flaps as documented herein.

Acknowledgments The financial support of the European Commission through the PELskin FP7 European project (AAT.2012.6.3-1—Breakthrough and emerging technologies) is greatly acknowledged. Funding of the position of Professor Christoph Brücker as the BAE SYSTEMS Sir Richard Olver Chair in Aeronautical Engineering is gratefully acknowledged

herein. AR acknowledges support from the UK Engineering and Physical Sciences Research Council under the project UK Consortium on Mesoscale Engineering Sciences (UKCOMES) (Grant No. EP/L00030X/1).

References

- Adrian R, Meinhart C, Tomkins C (2000) Vortex organization in the outer region of the turbulent boundary layer. *J Fluid Mech* 422:1–54
- Bhatnagar P, Gross E, Krook M (1954) A model for collision processes in gases. I: small amplitude processes in charged and neutral one-component system. *Phys Rev* 94:511–525
- Chandrasekaran V, Cain A, Nishida T, Cattafesta L, Sheplak M (2005) Dynamic calibration technique for thermal shear-stress sensors with mean flow. *Exp Fluids* 39:56–65

4. Chorin AJ (1968) Numerical solution of Navier–Stokes equations. *Math Comput* 22(104):745–762
5. Favier J, Dauplain A, Basso D, Bottaro A (2009) Passive separation control using a self-adaptive hairy coating. *J Fluid Mech* 627:451–483
6. Favier J, Revell A, Pinelli A (2013) A lattice Boltzmann-immersed boundary method to simulate the fluid interaction with moving and slender flexible objects. *J Comput Phys* 261:145–161
7. Favier J, Revell A, Pinelli A (2015) Numerical study of flapping filaments in a uniform fluid flow. *J Fluids Struct* 53:26–35
8. Finnigan JJ, Mulhearn PJ (1978a) Modelling waving crops in a wind tunnel. *Bound Layer Meteorol* 14:253–277
9. Finnigan JJ, Mulhearn PJ (1978b) A simple mathematical model of airflow in waving plant canopies. *Bound Layer Meteorol* 14:415–431
10. Guo Z, Zheng C, Shi B (2002) Discrete lattice effects on the forcing term in the lattice Boltzmann method. *Phys Rev E* 65(4):046308
11. Harlow FH, Welch E (1965) Numerical calculation of time-dependent viscous incompressible flow of fluid with free surface. *Phys Fluids* 8(12):2182–2189
12. Huang WX, Shin SJ, Sung HJ (2007) Simulation of flexible filaments in a uniform flow by the immersed boundary method. *J Comput Phys* 226(2):2206–2228
13. van Kan J (1986) A second-order accurate pressure correction scheme for viscous incompressible flow. *SIAM J Sci Stat Comput* 7(3):870–891
14. Kim J, Moin P (1985) Application of a fractional-step method to incompressible Navier–Stokes equations. *J Comput Phys* 59(2):308–323
15. Kunze S, Bruecker C (2012) Control of vortex shedding on a circular cylinder using self-adaptive hairy-flaps. *C R Mecanique* 340(1):41–56
16. Nepf HM (2012) Flow and transport in regions with aquatic vegetation. *Annu Rev Fluid Mech* 44:123–142
17. Nezu I, Okamoto T (2010) The effect of coherent waving motion on turbulence structure in flexible vegetated open channel flows. In: Proceedings of the international conference on Fluvial Hydraulics, River flow. Braunschweig, Germany, 8–10 Sept, pp 429–436
18. O’Connor J, Revell A, Mandal P, Day P (2016) Application of a lattice Boltzmann-immersed boundary method for fluid-filament dynamics and flow sensing. *J Biomech* 49(11):2143–2151
19. Peskin CS (1972) Flow patterns around heart valves: a numerical method. *J Comput Phys* 10(2):252–271
20. Peskin CS (2002) The immersed boundary method. *Acta Numer* 11:1–39
21. Pinelli A, Naqavi I, Piomelli U, Favier J (2010) Immersed-boundary methods for general finite-difference and finite-volume Navier–Stokes solvers. *J Comput Phys* 229(24):9073–9091
22. Py C, Langre E, Moulia B, Hemon P (2005) Measurement of wind-induced motion of crop canopies from digital video images. *Agric For Meteorol* 130:223–236
23. Py C, Langre E, Moulia B (2006) A frequency lock-in mechanism in the interaction between wind and crop canopies. *J Fluid Mech* 568:425–449
24. Qian Y, DHumieres D, Lallemand P (1992) Lattice bgk models for Navier–Stokes equation. *Europhys Lett* 17(6):479–484
25. Uhlmann M (2005) An immersed boundary method with direct forcing for the simulation of particulate flows. *J Comput Phys* 209(2):448–476